ACS OMEGA

http://pubs.acs.org/journal/acsodf

Article

High-Performance and High-Voltage Supercapacitors Based on N-Doped Mesoporous Activated Carbon Derived from Dragon Fruit Peels

Dayakar Gandla, Xudong Wu, Fuming Zhang, Chongrui Wu, and Daniel Q. Tan*

Cite This: *ACS Omega* 2021, 6, 7615−7625

Read Online

ACCESS | Metrics & More | Article Recommendations

ABSTRACT: Designing the mesopore-dominated activated carbon electrodes has witnessed a significant breakthrough in enhancing the electrolyte breakdown voltage and energy density of supercapacitors. Herein, we designed N-doped mesoporous-dominated hierarchical activated carbon (N-dfAC) from the dragon fruit peel, an abundant biomass precursor, under the synergetic effect of KOH as the activating agent and melamine as the dopant. The electrode with the optimum N-doping content (3.4 at. %) exhibits the highest specific capacitance of 427 F g^{-1} at 5 mA cm^{-2} and cyclic stability of 123% capacitance retention until 50000 charge−discharge cycles at 500 mA cm^{-2} in aqueous 6 M KOH electrolytes. We designed a 4 V symmetric coin cell supercapacitor cell, which exhibits a remarkable specific energy and specific power of 112 W h kg^{-1} and 3214 W kg^{-1}, respectively, in organic electrolytes. The cell also exhibits a significantly higher cycle life (109% capacitance retention) after 5000 GCD cycles at the working voltage of ≥3.5 V than commercial YP-50 AC (∼60% capacitance retention). The larger Debye length of the diffuse ion layer permitted by the mesopores can explain the higher voltage window, and the polar N-doped species in the dfAC enhance capacitance and ion transport. The results endow a new path to design high-capacity and high-working voltage EDLCs from eco-friendly and sustainable biomass materials by properly tuning their pore structures.

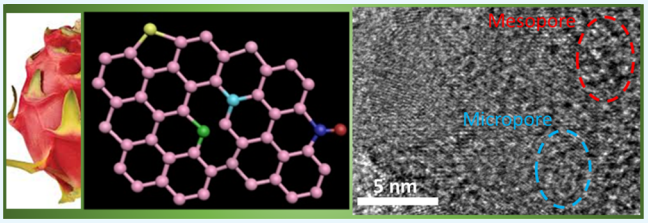

INTRODUCTION

The exigency for electric vehicles, portable equipment, and smart grids has emphatically stimulated the rapid development of electrochemical energy storage devices with sustainability, high energy density, and cost-effectiveness.[1−3] Electric double-layer capacitors (EDLCs) or ultracapacitors are a promising type of energy storage devices because of their reliable cycle life, faster charge/discharge rate, and remarkable power density.[4,5] Among the various EDLCs, porous activated carbon (AC) has been regarded as a prominent electrode material because of its high electrochemical stability, large surface area, rich porosity, and good electrical conductivity.[6,7] In general, AC materials are prepared using fossil-based chemical products as raw materials, which are expensive and cause environmental pollution.[8,9] In particular, these commercialized ACs are predominantly microporous (<1 nm) in nature, which do not allow high accessibility for large-sized ions of nonaqueous electrolytes and show inferior electrochemical performance at higher working voltages.

Consequently, researchers have a significant research interest in pursuing renewable and green biomass as carbon sources for high capacity and hierarchical pore structure. The biomass includes pineapple leaves,[10] chicken, eggshells,[11] neem leaves,[12] soybeans,[13] coconut shells,[14] walnut shells,[15] human hair,[16] and garlic skin.[17] However, the limited microporous surface area in many of the approaches impoverished the pore size distribution, the low packing density, the specific capacitance, and energy density of these AC-based electrodes. The inappropriate mesopore density further reduces the electronic conductivity by decreasing the ion transport rate during the charge−discharge process. Especially, the large solvated ions in organic electrolytes ultimately affect the power performance of AC-based supercapacitors.[18] Therefore, a great deal of research attention is focused on designing a hierarchical porous structure with controlled micro-and mesopore ratios to realize high specific capacitance, voltage window, specific energy, and specific power.

Recently, heteroatom doping, especially N-doping on biomass-derived carbon materials, has been proven to be effective in deriving the hierarchical pore structures and improving the surface wettability and ion transportation near

Received: December 18, 2020
Accepted: February 12, 2021
Published: March 9, 2021

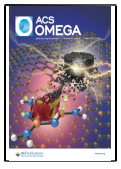

https://dx.doi.org/10.1021/acsomega.0c06171
ACS Omega 2021, 6, 7615−7625

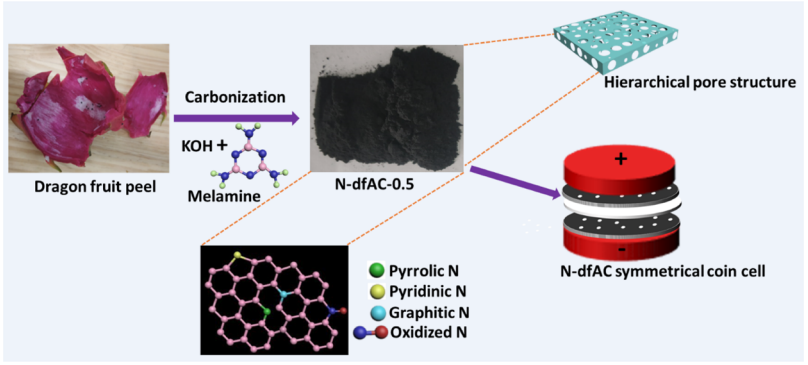

Figure 1. Schematic illustration of the synthesis of N-doped porous AC from a dragon fruit peel.

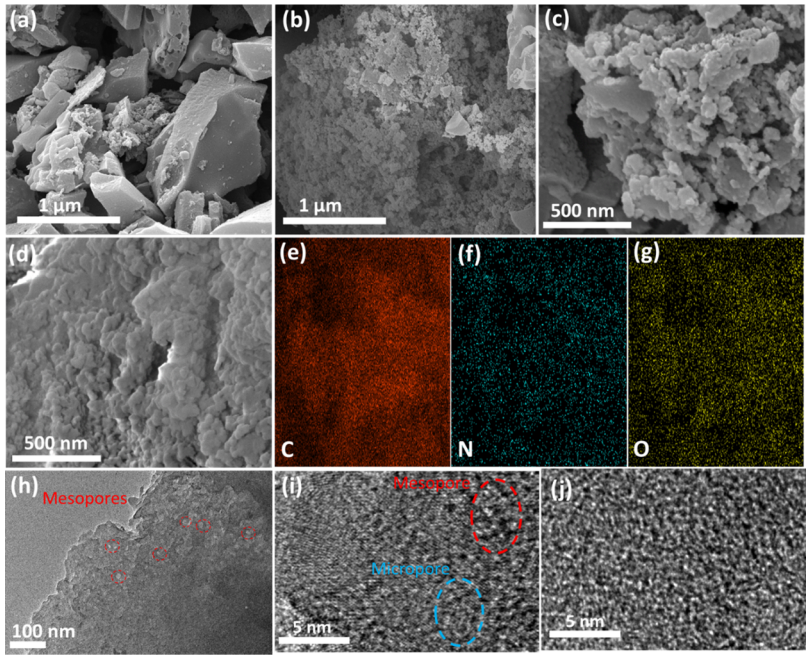

Figure 2. SEM images of (a) dfAC, (b) and (c) N-dfAC-0.5, and (d) N-dfAC-1. (e–g) EDS elemental mapping of C, N, and O elements in N-dfAC-0.5. (h–j) TEM images of N-dfAC-0.5 showing micro- and mesoporous structures.

the electrode–electrolyte interface.[19,20] Moreover, N-doped porous carbon materials exhibit pseudocapacitance through redox reaction, increasing their energy storage capacity.[21] An interesting phenomenon from these research studies is the achievement of hierarchical carbon structures with a high fraction of mesopores. Monte Carlo simulations on an AC-based slit-like pore model suggested that there is a correlation between the optimal pore width and working voltage. When larger solvated ion size organic or ionic liquids are employed as electrolytes, the working voltage increases with the increase in the optimal pore width.[22] Interestingly, the most recent studies also correlate with this theory. It appears that higher voltage is achievable by tuning the pore size to the mesopore scale (>2 nm).[23] Therefore, the heteroatom doping and the appropriate pore structure engineering point to the direction for a better design of next-generation EDLCs.

Herein, we have chosen the dragon fruit (*Hylocereus undatus*) peel for the first time as a different biowaste material to synthesize the N-doped mesopore-dominated AC (N-dfAC) for realizing the high performance supercapacitor. After carbonizing the raw material and the subsequent activation with KOH, the authors performed a simultaneous N-doping using melamine as an external nitrogen source. The authors found that moderate N-doping content of 3.4 at. % resulted in the highest specific surface area of 2667 m^2/g and appropriate pore size distribution with a high pore volume and pore diameter. In order to find the effect of the N-doping level on the electrochemical performance of AC supercapacitor, we first performed a three-electrode testing experiment in an aqueous electrolyte. Then, we designed the symmetric coin cell supercapacitor using the electrodes with an optimized N-doping level and pore structure, demonstrating a reliable cyclic stability and excellent specific energy at a high working voltage (≥3.5 V) in organic electrolytes.

RESULTS AND DISCUSSION

Microstructure and Surface Analysis. The carbonized carbon was mixed simultaneously with KOH for activation and melamine for doping and then heated at 800 °C for 2 h. The doping process finally yields N-dfAC, in which some of the carbon atoms are replaced by the various types of N atoms. The anticipated molecular configuration of N includes pyridinic N, pyrrolic N, graphitic or quaternary N, and oxidized N (Figure 1). The dfAC electrodes' morphology was

https://dx.doi.org/10.1021/acsomega.0c06171
ACS Omega 2021, 6, 7615–7625

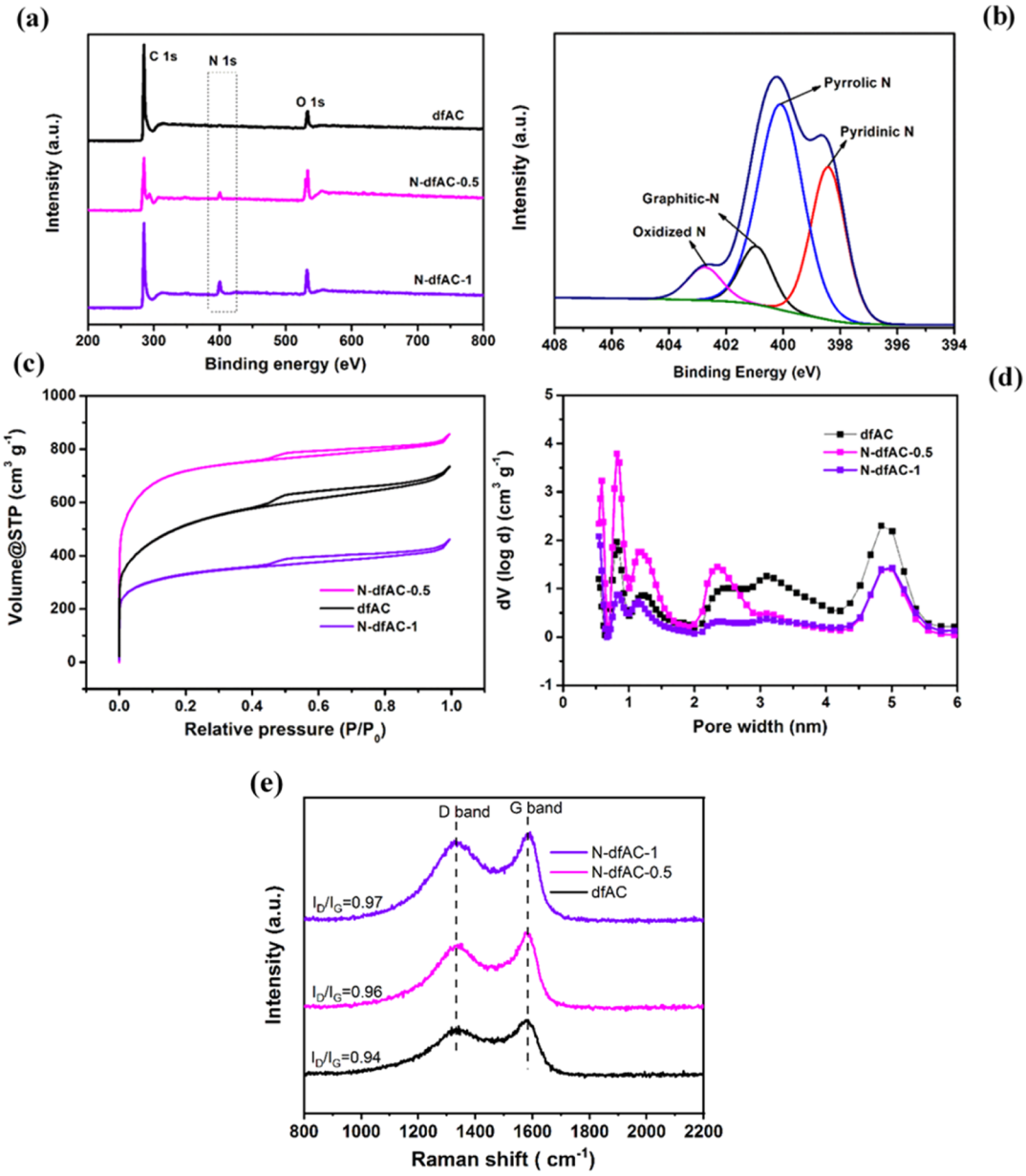

Figure 3. (a) XPS survey spectra of dfAC and N-dfACs and (b) high-resolution N 1s XPS spectrum of N-dfAC-0.5. (c) N_2 adsorption−desorption isotherms of dfAC and N-dfACs. (d) Pore size distributions from micropores to mesopores. (e) Raman spectra of dfAC, N-dfAC-0.5, and N-dfAC-1.

analyzed using scanning electron microscopy (SEM) before and after N-doping with the melamine. Without melamine, the carbonized dragon fruit peel using KOH can produce only bulk carbon particulates of several microns (Figure 2a). However, melamine addition during the KOH activation process results in a drastic change in the morphology (Figure 2b−d). At a lower amount of melamine (i.e., 0.5 wt %), the bulk carbon framework is converted to spherically aggregated porous nanoparticles. Upon increasing the amount of melamine to 1 wt %, the spherical aggregates formed an interconnected structure. The dragon fruit peel mainly consists of linoleic acid, oleic acid, and palmitic acid, which have high stability under the activation process. Therefore, KOH's sole contribution leads to an inefficient etching of the stable portion, resulting in a bulk morphology. The energy-dispersive X-ray (EDX) analysis confirms the homogeneous distribution of C (83.4 at. %), N (3.6 at. %), and O (13 at. %) elements in N-dfAC-0.5 (Figure 2e−g). The hierarchical porous AC structure is confirmed using transmission electron microscopy (TEM) (Figure 2h−j). The N-dfAC-0.5 shows abundant nano-sized mesopores beside subnano micropores. Such a mesopore-dominated hierarchical porous structure would bestow a unique advantage in shortening the ion diffusion path and enhancing the electrodes' energy storage capacity.[13,24]

The presence of the doped N atoms was further confirmed using X-ray photoelectron spectroscopy (XPS). Figure 3a shows the XPS survey spectra of N-dfAC-0.5 and N-dfAC-1, which reveal the occurrence of C, N, and O atoms. In N-dfAC-0.5, the content of C, N, and O was found to be 81.1, 3.4, and 15.5 at. %, respectively, which is consistent with the results obtained from EDX analysis. The presence of nitrogen in N-dfAC-0.5 and N-dfAC-1 improves their wettability with the electrolyte, enhancing the accessibility of the electrolyte ions and thus the increased charge storage capacity.[25]

https://dx.doi.org/10.1021/acsomega.0c06171
ACS Omega 2021, 6, 7615−7625

The high-resolution N 1s spectra of N-dfAC-0.5 (Figure 3b) are deconvoluted into four peaks corresponding to pyridinic N (398.4 eV), pyrrolic N (400.1 eV), graphitic or quaternary N (400.95 eV), and oxidized N (402.75 eV), as summarized in Table 1.[26] The graphitic N aids in enhancing the electron migration rate, thereby increasing carbon electrodes' conductivity.[21,27] Although the N content in N-dfAC-0.5 (3.4 at. %) is lower than that of N-dfAC-1 (7.9 at. %), it has higher atomic % of pyrrolic N, graphitic N, and oxidized N, leading to a superior electrochemical performance;[28] therefore, the charge storage capacity of N-dfAC-0.5 is higher.

Table 1. Concentration of Nitrogen Configuration in N-dfACs

	atomic % of total N			
sample	pyridinic N	pyrrolic N	graphitic N	oxidized N
N-dfAC-0.5	30.15	52.38	10.9	6.57
N-dfAC-1	54.56	30.11	9.56	5.78

The effect of the melamine-assisted N doping on the specific surface area was investigated by the BET method and pore size distribution by DFT and BJH methods (Figure 3c), which is summarized in Table 2. The specific surface areas of dfAC, N-dfAC-0.5, and N-dfAC-1 were found to be 2994, 2667, and 2134 $m^2 g^{-1}$, respectively, along with the pore volumes (DFT) of 1.19, 1.18, and 0.62 $cm^3 g^{-1}$, respectively. The pore size distribution curve (Figure 3d) of the dfAC and N-dfAC implies the broad pore distribution between 0.5 and 5.5 nm in size, which indicates the presence of a hierarchical porous structure with dual micro- and mesopores. Especially, the abundant mesopores endow more charge storage sites and more ion diffusion channels. Such a pore structure may endow enhanced conductivity, voltage window, and power performance of supercapacitors when employing larger ion-sized organic electrolyte or ionic liquid.[29] The lower pore volume in N-dfAC-1 is possibly due to the high concentration of N functionalities on the surface of carbon, which etches in the vicinity of pore surfaces.

Table 2. Specific Surface Area and Pore Structure Parameters of dfAC and N-dfACs

sample	SBET ($m^2 g^{-1}$)	DBJH (nm)	DDFT (nm)	VBJH ($cm^3 g^{-1}$)	VDFT ($cm^3 g^{-1}$)
dfAC	2994	3.02	0.55	0.3	1.19
N-dfAC-0.5	2667	3.14	0.59	0.21	1.18
N-dfAC-1	2134	3.14	0.56	0.2	0.62

The specific surface area and pore characteristics are pivotal for electrochemical energy storage. Figure 3c represents the N_2 adsorption−desorption isotherms of the dfAC, N-dfAC-0.5, and N-dfAC-1. All the samples exhibit type I and type IV isotherms, the sharp adsorption at a lower relative pressure revealing the presence of micropores, whereas the hysteresis loop at a higher relative pressure (0.4−0.7) implies the existence of mesopores. This is denoted as the H4 type hysteresis loop with slit-shaped pores. The formation of the hysteresis loop of N_2 adsorption−desorption is explained by filling mesopores by capillary condensation at high relative pressure (P/P_0) followed by pore emptying by an evaporation process.

The degree of graphitization of the synthesized porous carbon materials was analyzed using Raman spectra. As shown in Figure 3e, the D band at 1336 cm^{-1} represents the disordered or defective structure of the carbon, whereas the G band at 1580 cm^{-1} represents the E_{2g} phonon vibration of the graphitic sp^2 hybridized carbon atoms.[30] The intensity ratio of D band to G band (I_D/I_G) reflects the degree of graphitization. The calculated I_D/I_G values of the dfAC, N-dfAC-0.5, and N-dfAC-1 are 0.94, 0.96, and 0.97, respectively. These results demonstrate that the graphitization degree was slightly decreased after N-doping which introduces defects in the form of N functionalities.

Electrochemical Performance Evaluation. Electrochemical performance can demonstrate the advantages of the N-doping and hierarchical pore structure. When employing the aqueous 6 M KOH electrolyte in a three-electrode system within the potential limit of −1 to 0 V, the dfAC and N-doped dfAC (N-dfAC-0.5 and N-dfAC-1) show the increase in the current-carrying capability with N-doping (Figure 4a). At a scan rate of 50 mV s^{-1}, the 0.5% doping results in the larger CV current, while the 1% doping leads to a decline in the area under CV curves. This difference confirms that the N-dfAC-0.5 electrode has the highest capacitive nature among the synthesized electrodes. N-dfAC-0.5 exhibits quasirectangular-shaped CV curves at various scan rates from 5 to 100 mV s^{-1} without any significant distortion in the peak shape (Figure 4b), demonstrating the high rate capability. As illustrated in Figure 4c, all the synthesized electrodes exhibit symmetrical and triangular-shaped GCD curves at the current density of 5 mA cm^{-2}, which characteristically features a typical EDLC. The N-dfAC-0.5 delivers a longer discharge time than the dfAC and N-dfAC-1, reflecting its high charge storage capacity. Moreover, the reversible electrochemical behavior of the N-dfAC-0.5 electrode is further confirmed by its fair symmetrical shape GCD curves at different current densities from 5 to 100 mA cm^{-2} with a negligible IR drop (Figure 4d).

The comparative specific capacitances of the undoped dfAC and N-doped dfAC electrodes at various current densities are represented in Figure 4e. At a current density of 5 mA cm^{-2}, the specific capacitances of the dfAC, N-dfAC-0.5, and N-dfAC-1 are 198, 427, and 350 F g^{-1}, respectively. N-doping extraordinarily increases the specific capacitance. Even at a higher current density of 100 mA cm^{-2}, the N-dfAC-0.5 exhibits a high rate capability with 80.3% capacitance retention (343 F g^{-1}). The higher specific capacitance of N-dfAC-0.5 in comparison with N-dfAC-1 is attributed to its high specific surface area, high pore volume, and high atomic percentage of pyrrolic N, graphitic N, and oxidized N, which lead to the enhanced ion diffusion and charge storage capacity.

To study the kinetics of ion transport across the electrode−electrolyte interface and conductive nature of the electrodes, electrochemical impedance spectroscopy (EIS) was performed in the frequency range of 10 kHz to 0.01 Hz (Figure 5a), and the corresponding equivalent circuit model to study the EIS is represented in the inset. Here, R_{ct} is the charge transfer resistance obtained from the diameter of the semicircle arc at high frequency, R_s represents the equivalent series resistance, CPE describes a constant phase element, and Z_w is the Warburg resistance for the diffusion of electrolyte ions toward the porous carbon.[31,32] The synthesized electrodes exhibited a small semicircle at high frequency, followed by a linear part parallel to the imaginary axis at the low-frequency region, implying their ideal capacitive nature. According to the fitted

https://dx.doi.org/10.1021/acsomega.0c06171
ACS Omega 2021, 6, 7615−7625

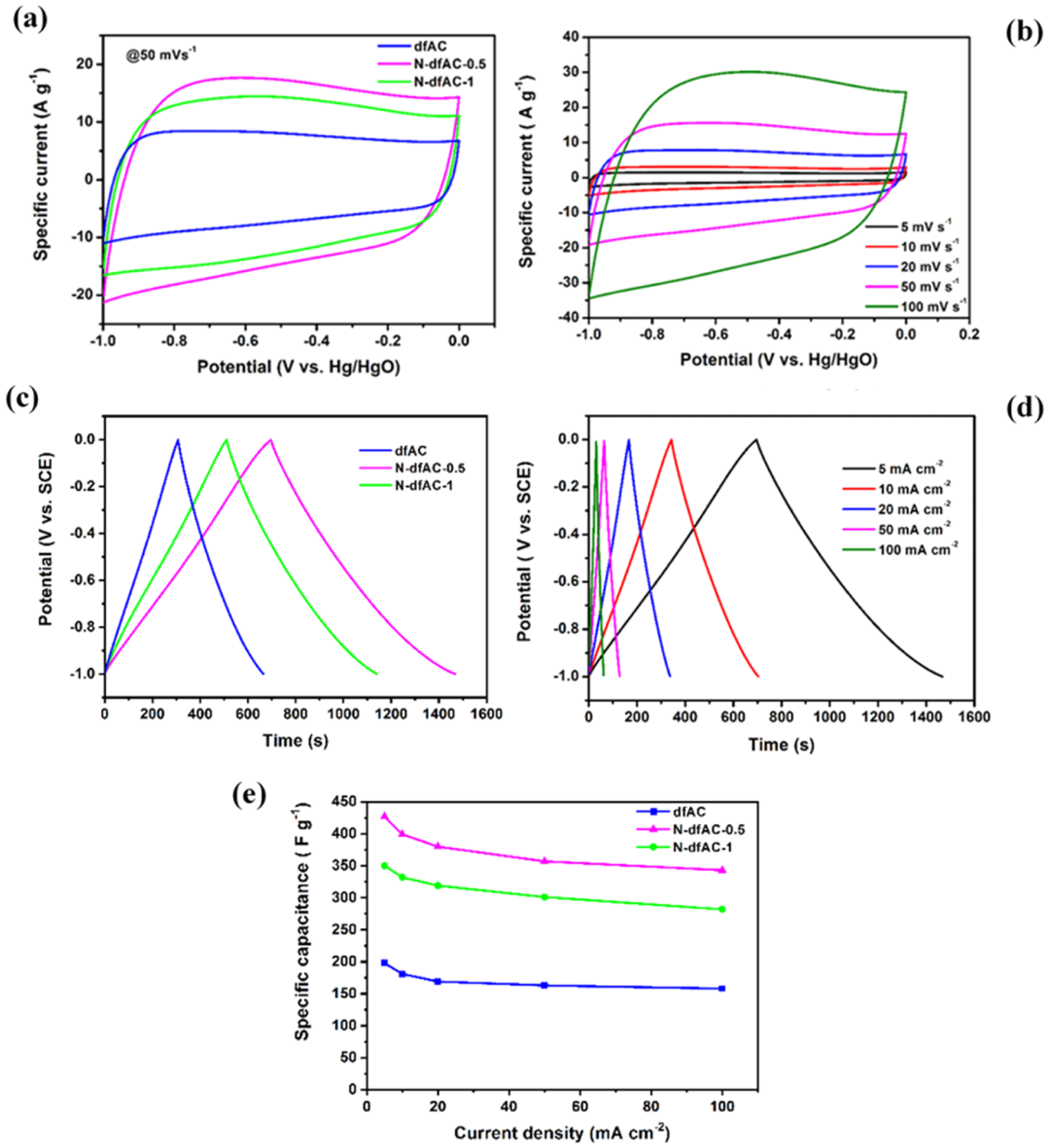

Figure 4. (a) Comparative CV curves of the dfAC, N-dfAC-0.5, and N-dfAC-1 at a scan rate of 50 mV s^{-1} (b) CV curves of N-dfAC-0.5 at different scan rates from 5 to 100 mV s^{-1} (c) GCD graphs of the dfAC, N-dfAC-0.5, and N-dfAC-1 at a current density of 5 mA cm^{-2}. (d) GCD curves of N-dfAC-0.5 at various current densities from 5 to 100 mA cm^{-2}. (e) Specific capacitance of dfAC and N-dfACs at different current densities.

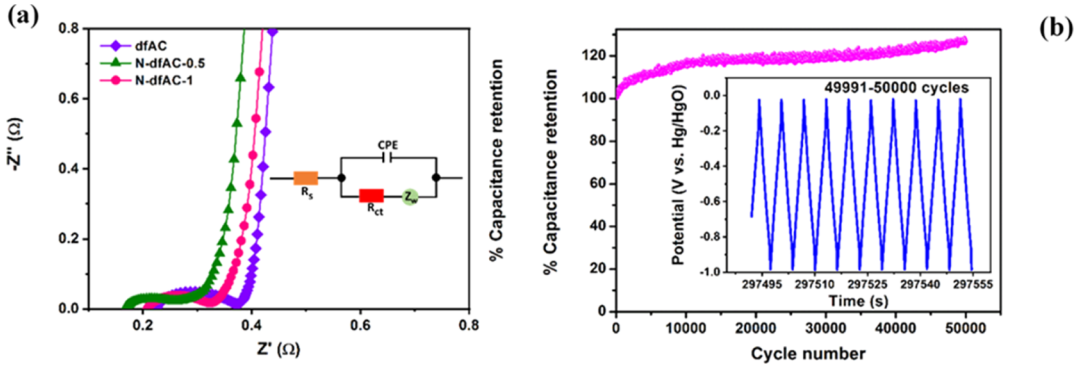

Figure 5. (a) Nyquist plots of the dfAC, N-dfAC-0.5, and N-dfAC-1; inset is the equivalent circuit model to analyze the impedance data. (b) Cycle life of the N-dfAC-0.5 electrode up to 50,000 GCD cycles at 500 mA cm^{-2} constant current density; the inset shows the shape of GCD curves for last 10 cycles.

https://dx.doi.org/10.1021/acsomega.0c06171
ACS Omega 2021, 6, 7615−7625

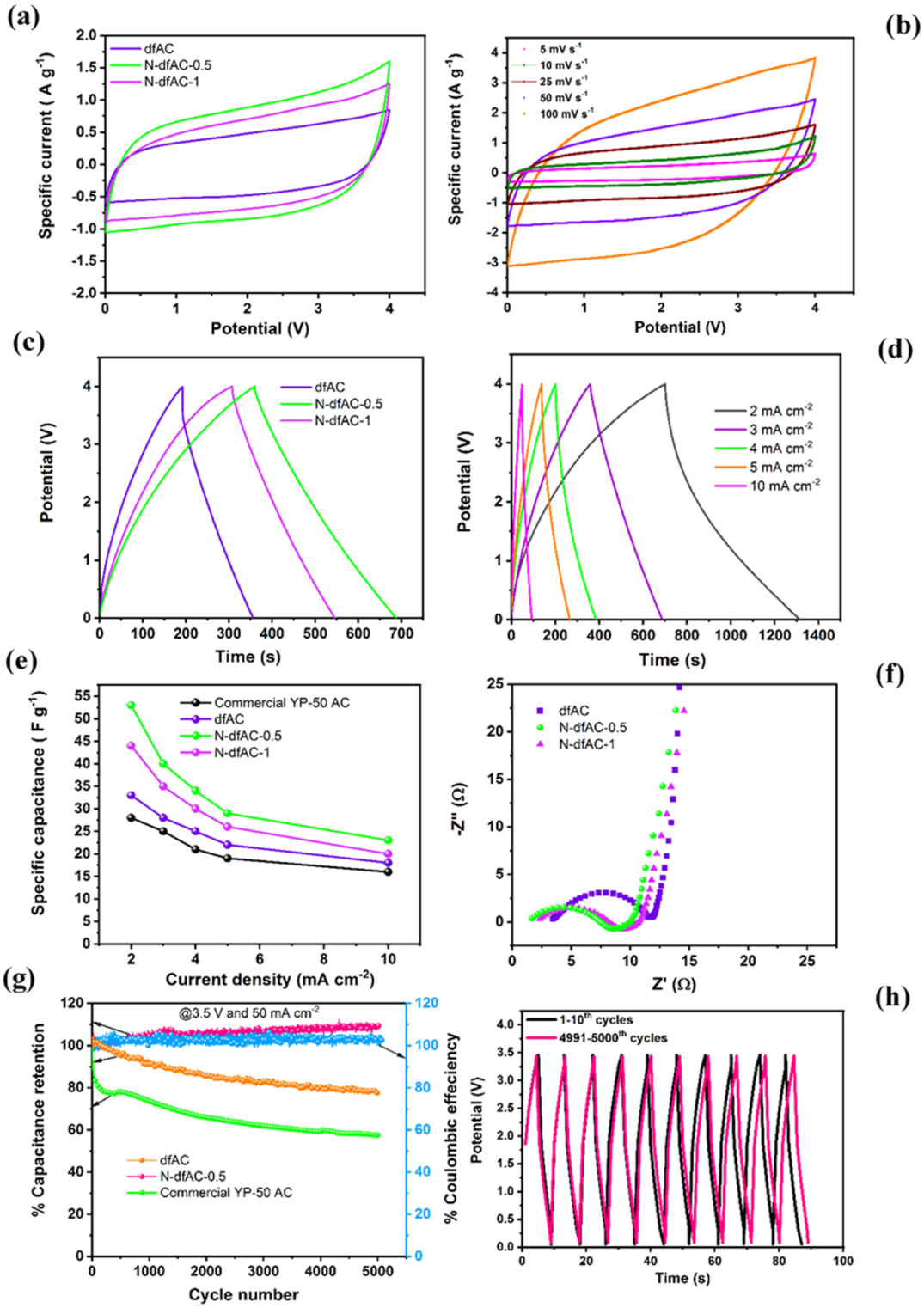

Figure 6. Electrochemical performance of the dfAC and N-doped dfAC supercapacitor devices in 1 M $TEABF_4$/acetonitrile organic electrolytes. (a) Comparative CV curves at a scan rate of 25 mV s^{-1}. (b) CV curves of the N-dfAC-0.5 at different scan rates. (c) Comparative GCD graphs at a current density of 3 mA cm^{-2}. (d) GCD curves of the N-dfAC-0.5 at various current densities. (e) Rate capability at different current densities. (f) Nyquist plots. (g) Capacitance retention and coulombic efficiency measured at 3.5 V and at a current density 50 mA cm^{-2}. (h) Shape of GCD curves of the N-dfAC-0.5 cell for first and last 10 cycles.

impedance data, N-dfAC-0.5 exhibits lower R_s (0.16 Ω) and R_{ct} (0.11 Ω) values than those of N-dfAC-1 (R_s = 0.20 Ω; R_{ct} = 0.12 Ω) and dfAC (R_s = 0.22 Ω; R_{ct} = 0.15 Ω). This comparison demonstrates that N-dfAC-0.5 has the lowest electrolyte ions diffusion resistance, charge transfer resistance, and excellent capacitive behavior, which are correlated with the results obtained from CV and GCD. The lower R_s and higher specific capacitance of N-dfAC-0.5 are attributed to the optimal pore structure and high atomic % of pyrrolic N, graphitic N, and oxidized N. The easy ion diffusion and the

https://dx.doi.org/10.1021/acsomega.0c06171
ACS Omega 2021, 6, 7615−7625

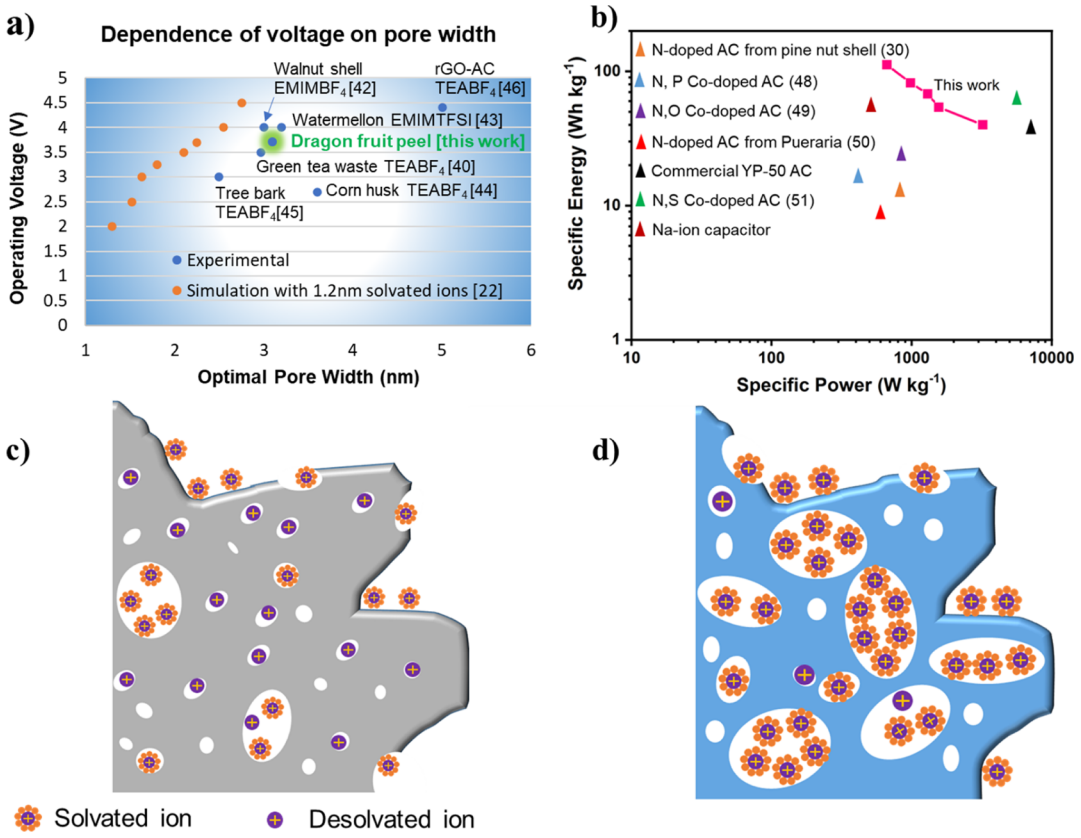

Figure 7. (a) Effect of optimal pore width on the working voltage of EDLC made of various carbon electrodes published. (b) Ragone plot showing the specific energy vs specific power of N-dfAC-0.5 in comparison with the reported carbon-based symmetric supercapacitors. (c,d) Schematic illustration of 2D projected views of small and large ions accessing to micro- and mesopores of commercial YP-50F AC and hierarchical AC, respectively.

enhanced conductivity in the electrolyte thereby result in the increased charge storage capacity.[33]

The long-term cyclic stability is a significant factor of the electrode material to realize its practical application as a supercapacitor. Figure 5b demonstrated the cyclic stability of the optimized electrode N-dfAC-0.5 using galvanostatic charge−discharge test (GCD). After cycling the cells for 50,000 cycles at a high current density of 500 mA cm^{-2}, the electrode still shows an exceptionally high capacitance retention of 123% and the symmetrical triangular shape on the GCD curves (inset of Figure 5b). The high capacitance retention is attributed to gradual activation and wetting of the N-doped porous carbon electrode with the electrolytes during prolonged charge−discharge process. This enhanced wettability endows better accessibility of electrolyte ions toward the micro- and mesopores of the carbon electrode and thereby results in the increase in the charge retention during cycling process. Such an exceptional capacitance retention higher than 100% has already been observed for some of the porous carbon-based electrodes.[34−36]

Besides, the larger mesoporous structure constructed within the dfAC materials also plays a favorable role for the high specific energy when employing organic electrolytes. Conventionally, the solvated ions from organic electrolytes are large and find it difficult to completely access the micropores (≤1 nm) in ACs, which are mostly unable to sustain voltages higher than 2.7 V. On the contrary, the mesopore-dominated N-dfAC provides an easy path and accessibility for the large organic ions. The electrochemical properties of the dfAC and N-doped dfACs were evaluated by designing symmetrical coin cell supercapacitors in the 1 M $TEABF_4$/acetonitrile electrolyte. Compared to dfAC, the N-doped dfACs, especially N-dfAC-0.5, showed the better charge storage behavior, which is evidenced by the highest current under CV curve (Figure 6a). As shown in Figure 6b, the N-dfAC-0.5 symmetric supercapacitor's CV curves show a quasirectangular shape at various scan rates under a high potential window of 4 V. At a high scan rate of 100 mV s^{-1}, the shape of the CV curve is slightly distorted. Although both dfAC and N-doped dfACs exhibited symmetrical and triangular-shaped GCD curves at a current density of 3 mA cm^{-2} (Figure 6c), the dfAC showed a large IR drop at the beginning of the discharge curve and shorter discharge time. However, N-doping significantly reduced the IR drop and increased the discharge time. This result demonstrates that N-doping increased both conductivity and specific capacitance of the material. The N-dfAC-0.5 delivers a longer discharge time than the dfAC and N-dfAC-1, reflecting its high charge storage capacity. The shape of GCD curves of N-dffAC-0.5 exhibited a different behavior at various current densities under 4 V (Figure 6d). At a low current density of 2 mA cm^{-2}, there is deviation from the linear triangular shape with low coulombic efficiency (i.e., more charge duration than discharge duration). The lower coulombic efficiency at low current density may be ascribed to the higher ratio of the parasitic side-chain reactions between the electrode and impurities present in the electrolyte.[37] However, when the current density increases from 3 to 10 mA cm^{-2}, the shape of GCD curves becomes nearly symmetric, indicating the high

https://dx.doi.org/10.1021/acsomega.0c06171
ACS Omega 2021, 6, 7615−7625

coulombic efficiency and reversible capacitive nature. Indeed, it showed 100% coulombic efficiency even at a high current density of 50 mA cm^{-2} (Figure 6g). The specific capacitance obtained by the N-dfAC-0.5 device is superior with respect to dfAC, N-dfAC-1, and YP-50 AC devices at various current densities (Figure 6e), which is mainly attributed to optimum doping content, which facilitates increased accessibility of bulky solvated ions into the mesopores, rendering a high charge storage capacity. The effect of N-doping on the conductive behavior of the dfAC is studied in organic electrolytes also using the Nyquist plot of the impedance data, as shown in Figure 6f. R_s values of the dfAC, N-dfAC-0.5, and N-dfAC-1 were calculated to be 3.43, 1.66, and 2.3 Ω, respectively. Moreover, the R_{ct} values were 8.11, 6.6, and 6.8 Ω, respectively. This apparently reveals an optimum N-doping content at 0.5 wt % that offers a better conductivity for faster ion diffusion through pore channels and thus a high specific power for the designed supercapacitor.

Relationship between Pore Size and Working Voltage. The supercapacitor's cyclic stability at high working voltages is crucial to realize its practical application in energy storage devices. The enhanced voltage withstanding capability was achieved when employing a mesoporous structured carbon electrode derived from green tea waste.[38] The microporous dominated commercial YP-50 AC cell exhibited only ∼60% capacitance retention after 5000 GCD cycles at 3.5 V and 50 mA cm^{-2} current density. This is due to inaccessibility of larger sized TEA^+ and BF_4^- ions of the electrolyte into the smaller pores, which diminishes the charge retention during the cycling process. However, employing the mesoporous dominated dfAC delivers a capacitance retention of 79% owing to more ion accessibility. Interestingly, after N-doping, the optimized N-dfAC-0.5 cell exhibited a remarkable cycle life with a capacitance retention of 109% and a high coulombic efficiency under the same test protocol as well (Figure 6g).

The mechanism for the enhanced capacitive behavior of dfAC with N-doping in the $TEABF_4$/acetonitrile organic electrolyte can be correlated to a recent study by Dai et al.[39] The authors performed a systematic investigation to analyze interactions of the cation (TEA^+) and anion (BF_4^-) of organic electrolytes with various carbon surface models (undoped carbon, pyrrolic-N modified carbon surface, graphitic-N modified carbon surface, and pyridine-N modified carbon surface). Introduction of electron-rich N species into carbon structures causes uneven electrostatic potentials and atomic charge distributions, leading to the surface polarization. Compared to undoped carbon, the adsorption energies of TEA^+ and BF_4^- ions gradually increased for various N-doped carbon models, and this higher adsorption energy indicates stronger attraction or affinity between the electrolyte ions and N-doped carbon surface. Such a strong affinity enhances the wettability of electrodes and facilitates electrolyte ion diffusion across the electrical double layer, which ultimately increases the energy storage performance of a supercapacitor.

The shape of the GCD curves of N-dfAC-0.5 is almost similar during the entire cycling process without any significant distortion. The representative curves of the first 10 and last 10 cycles are shown (Figure 6h). This superior performance at high voltage is in good agreement with the Monte Carlo simulations on the AC-based slit-like pore model for larger solvated ions. The model proved that wider mesopores are preferred over narrower micropores for higher voltage operation.

Figure 7a displays the dependence of working voltage on the pore size of N-dfAC-0.5, various ACs, and previous simulations.[22,38,40−44] The relationship further manifests the importance of large pores and their utilization trend for high-performance supercapacitors. When the dominant pores are larger than 1.5 nm, the EDLCs may render a higher working voltage than those using microporous AC electrodes. The hierarchical micropore- and mesopore-dominated carbon structures are schematically represented in Figure 7c,d, respectively. In the former case, because of predominant micropores and limited mesopores, only smaller sized ions from aqueous electrolytes can be accessible. There is restricted access for large-sized solvated ions or desolvated ions from organic or ionic liquid electrolytes, which renders a high charge storage capacity and a low working voltage. In the latter case, because of the presence of predominant mesopores, in addition to small-sized ions, the large-sized solvated ions can also be easily entered into the pores, which endow not only high charge storage capacity but also higher working voltage. This preferred distribution of the large ions results in a thicker diffuse layer (λ_D) and thus a higher accumulated charge quantity. According to the Gouy−Chapman−Stern model, the working voltage is proportional to the pore width and charges.[45] Consequently, the mesopore-dominated AC can be operated at a higher working voltage with an enhanced cyclic retention comparing with the micropore-dominated AC.

The advantage of a higher working voltage is reflected in the increased specific energy and specific power of the device. The Ragone plot (Figure 7b) shows that the 4 V device delivers a remarkable specific energy of 112 W h kg^{-1} at a specific power of 664 W kg^{-1}, which is measured at a current density of 2 mA cm^{-2} and the obtained specific capacitance value is 53 F g^{-1}. At a current density of 10 mA cm^{-2}, the device delivers a high specific power of 3214 W kg^{-1} at a specific energy of 40 W h kg^{-1} and the obtained specific capacitance value is 23 F g^{-1}. The achieved specific energy of 112 W h kg^{-1} is higher than the reported heteroatom-doped ACs and commercial YP-50F−based capacitors.[28,46−49]

CONCLUSIONS

Mesopore-dominated N-doped carbon (N-dfAC) is synthesized using the eco-friendly dragon fruit peel as a precursor through a facile two-step process, that is, carbonization followed by simultaneous KOH activation and melamine doping. The structural nature of a large specific surface area (2667 m^2 g^{-1}), appropriate pore size distribution, and optimal N-doping level (3.4 at. %) endow the N-dfAC-0.5 electrode with a high specific capacitance and a cycle life in an aqueous electrolyte in a three-electrode system. The N-doping significantly enhanced the charge storage capacity and conductivity of dfAC. The N-dfAC-0.5−based symmetric coin cell using an organic electrolyte exhibited an extraordinary cycle life, high specific energy, and specific power at a higher voltage of ≥3.5 V. The results benefit from the accommodation of more ionic charges of the large mesopores and the formation of a more extensive diffuse layer according to the modified Gouy−Chapman−Stern model. This study demonstrates an engineering pathway to achieve high voltage and power density through N-doping and mesopores' synergistic effort in AC electrodes.

https://dx.doi.org/10.1021/acsomega.0c06171
ACS Omega 2021, 6, 7615−7625

EXPERIMENTAL SECTION

Materials. The dragon fruit (raw material) was purchased from the local fruit market. All chemicals were obtained from Shanghai Macklin Biochemical Co., Ltd and were used without further purification.

Synthesis of N-dfACs. First, the dragon fruit peels were washed with the DI water, followed by ethanol to eliminate the surface impurities before drying at 65 °C for 12 h. Subsequently, it was crushed into powder and sieved under the size of 500 μm. The obtained powder was carbonized at 600 °C (at a heating rate of 5 °C min^{-1}) for 2 h in the presence of argon gas in a tube furnace. Then, the fine powders, KOH, and melamine were mixed at different mass ratios (1:3:0, 1:3:0.5, and 1:3:1) and annealed at 800 °C for 2 h for an activation treatment. Afterward, the obtained powders were washed with a 1 M HCl solution, followed by the DI water to remove the captured potassium compounds and other surface impurities. Finally, it was dried at 85 °C for 12 h to obtain an N-doped porous AC. The dfACs synthesized at different weight ratios of melamine dopant are marked as N-dfAC-0.5 and N-dfAC-1.

Characterizations. The surface morphology of the synthesized samples was investigated using a ZEISS Sigma-500 scanning electron microscope (Germany). The elemental distribution and mapping were obtained using Energy Dispersive Spectroscopy (EDS, BRUKE XFlash-6130, Germany). TEM images were captured on a JEM2100 instrument at an acceleration voltage of 200 kV. The surface elemental composition was evaluated using XPS from Thermo Scientific ESCALAB 250Xi, USA, with a monochrome Al Kα as the X-ray source. The N_2 adsorption−desorption isotherm analysis of the samples was performed by a Quantachrome Autosorb-iQ2-MP (USA) Nova-1000 system at −196 °C. The degassing of the samples was performed at 250 °C for 3 h. The specific surface and pore size distribution were analyzed using Brunauer−Emmett−Teller (BET) and density functional theory (DFT) methods, respectively.

Electrochemical Performance Test. The electrochemical performance of the synthesized N-dfAC materials was measured in a three-electrode cell using the Gamry electrochemical workstation (Interface 1010E, USA). The working electrodes were prepared by homogeneously mixing N-dfAC (85%), super P carbon black (10%), and polyvinylidene difluoride (5%) in N-methyl-2-pyrrolidinone solution, followed by coating on a 1 cm × 1 cm nickel foam and subsequent drying in an oven at 85 °C for 12 h. Finally, it was pressed into a dense sheet at 10 MPa for 60 s to obtain working electrodes. The loaded active mass of N-dfAC working electrodes was ∼9 mg cm^{-2}. Hg/HgO was used as the reference, and a Pt plate was used as counter electrodes. 6 M aqueous KOH solution was used as the electrolyte. Cyclic voltammetry (CV) measurement was carried out at different scan rates from 5 to 100 mV s^{-1}, the voltage window for CV and galvanostatic charge−discharge (GCD) measurements is in the range of −1 to 0 V, and the current density for GCD measurements is varied from 5 to 100 mA cm^{-2}. EIS data were recorded with 5 mV amplitude potential within 10 kHz to 0.01 Hz frequency range.

The specific capacitance values in the three-electrode system were calculated using GCD curves from the following equation[50]

$$C = \frac{I\Delta t}{m\Delta V} \quad (1)$$

where C denotes the specific capacitance (F g^{-1}) of the electrode materials, I represents the discharge current (A), Δt is the discharge time (s), m is the mass (g) of active material loaded, and ΔV denotes the potential window (V) excluding IR drop.

A symmetrical supercapacitor device was fabricated using CR2032 coin cells to verify the practical applicability of electrode materials. The optimized N-dfAC-0.5 was used as both anode and cathode. Aluminum foil of 0.2 μm thickness was used as a current collector. 1 M $TEABF_4$/acetonitrile was employed as an electrolyte, and a 35 μm thick cellulose NKK TF4035 (Nippon Kodoshi, Japan), having 75% porosity, was used as a separator. The specific capacitance of the supercapacitor cell was calculated from eq 1. The total loaded mass (in g) of both the anode and cathode electrodes is taken into consideration.

The specific energy (E, W h kg^{-1}) and specific power (P, W kg^{-1}) of the supercapacitor device were calculated from the following equations.[50]

$$E = \frac{C \times \Delta V^2}{2 \times 3.6} \quad (2)$$

$$P = \frac{E \times 3600}{\Delta t} \quad (3)$$

where C denotes the specific capacitance (F g^{-1}) of the device, ΔV describes the potential window (V) excluding IR drop, and Δt is the discharge time (s).

AUTHOR INFORMATION

Corresponding Author

Daniel Q. Tan − *Guangdong Technion Israel Institute of Technology, Shantou, Guangdong 515063, China;* orcid.org/0000-0002-2282-2000; Email: daniel.tan@gtiit.edu.cn

Authors

Dayakar Gandla − *Guangdong Technion Israel Institute of Technology, Shantou, Guangdong 515063, China*

Xudong Wu − *Guangdong Technion Israel Institute of Technology, Shantou, Guangdong 515063, China*

Fuming Zhang − *Guangdong Technion Israel Institute of Technology, Shantou, Guangdong 515063, China*

Chongrui Wu − *Guangdong Technion Israel Institute of Technology, Shantou, Guangdong 515063, China*

Complete contact information is available at: https://pubs.acs.org/10.1021/acsomega.0c06171

Notes

The authors declare no competing financial interest.

ACKNOWLEDGMENTS

This research was supported by 2020 Li Ka Shing Foundation Cross-Disciplinary Research grant 2020LKSFG01A and the Guangdong-Israel Special Research grant 200902154890781. Dr. Guanghui Song's help with sample handling for characterization is appreciated.

https://dx.doi.org/10.1021/acsomega.0c06171
ACS Omega 2021, 6, 7615−7625

REFERENCES

(1) Qin, J.; Sari, H. M. K.; Wang, X.; Yang, H.; Zhang, J.; Li, X. Controlled Design of Metal Oxide-based (Mn^{2+}/Nb^{5+}) Anodes for Superior Sodium-ion Hybrid Supercapacitors: Synergistic Mechanisms of Hybrid Ion Storage. *Nano Energy* **2020**, *71*, 104594.

(2) Wang, Y.; Wang, X.; Li, X.; Li, X.; Liu, Y.; Bai, Y.; Xiao, H.; Yuan, G. A High-Performance, Tailorable, Wearable, and Foldable Solid-State Supercapacitor Enabled by Arranging Pseudocapacitive Groups and MXene Flakes on Textile Electrode Surface. *Adv. Funct. Mater.* **2020**, *31*, 2008185.

(3) Xiong, D.; Li, X.; Bai, Z.; Lu, S. Recent Advances in Layered $Ti_3C_2T_x$ MXenes for Electrochemical Energy Storage. *Small* **2018**, *14*, 1703419.

(4) Zhang, J. M.; Hua, Q.; Li, J.; Yuan, J.; Peijs, T.; Dai, Z.; Zhang, Y.; Zheng, Z.; Zheng, L.; Tang, J. Cellulose-derived highly porous three-dimensional activated carbons for supercapacitors. *ACS Omega* **2018**, *3*, 14933.

(5) Liu, X.; Ma, C.; Jiaxin, L.; Beata, Z.; Ryszars, K.; Xuecheng, C.; Paul, K.; Tao, T.; Ewa, M. Biomass-derived robust three-dimensional porous carbons for high volumetric performance supercapacitors. *J. Power Sources* **2019**, *412*, 1.

(6) Yao, F.; Pham, D. T.; Lee, Y. H. Carbon-based materials for lithium-ion batteries, electrochemical capacitors, and their hybrid devices. *ChemSusChem* **2015**, *8*, 2284.

(7) Cao, Y.; Wang, K.; Wang, X.; Gu, Z.; Fan, Q.; Gibbons, W.; Hoefelmeyer, J. D.; Kharel, P. R.; Shrestha, M. Hierarchical porous activated carbon for supercapacitor derived from corn stalk core by potassium hydroxide activation. *Electrochim. Acta* **2016**, *212*, 839.

(8) Wang, C.; Wu, D.; Hongju, W.; Zhiyong, G.; Fang, X.; Kai, J. A green and scalable route to yield porous carbon sheets from biomass for supercapacitors with high capacity. *J. Mater. Chem. A* **2018**, *6*, 1244.

(9) Shan, D.; Yang, J.; Liu, W.; Jun, Y.; Zhuagjun, F. Biomass-derived three-dimensional honeycomb-like hierarchical structured carbon for ultrahigh energy density asymmetric supercapacitors. *J. Mater. Chem. A* **2016**, *4*, 13589.

(10) Sodtipinta, J.; Amornsakchai, T.; Pakawatpanurut, P. Nanoporous carbon derived from agro-waste pineapple leaves for supercapacitor electrode. *Adv. Nat. Sci.* **2017**, *8*, 035017.

(11) Gao, F.; Qu, J.; Zhao, Z.; Wang, Z.; Qiu, J. Nitrogen-doped activated carbon derived from prawn shells forhigh-performance supercapacitors. *Electrochim. Acta* **2016**, *190*, 1134.

(12) Ahmed, S.; Parvaz, M.; Johari, R.; Rafat, M. Studies on activated carbon derived from neem (azadirachta indica) bio-waste, and its application as supercapacitor electrode. *Mater. Res. Express* **2018**, *5*, 045601.

(13) Long, C.; Jiang, L.; Wu, X.; Jiang, Y.; Yang, D.; Wang, C.; Wei, T.; Fan, Z. Facile synthesis of functionalized porous carbon with three-dimensional interconnected pore structure for high volumetric performance supercapacitors. *Carbon* **2015**, *93*, 412−420.

(14) Xia, J.; Zhang, N.; Chong, S.; Li, D.; Chen, Y.; Sun, C. Three-dimensional porous graphene-like sheets synthesized from biocarbon via low-temperature graphitization for a supercapacitor. *Green Chem.* **2018**, *20*, 694.

(15) Fu, H.-H.; Chen, L.; Gao, H.; Yu, X.; Hou, J.; Wang, G.; Yu, F.; Li, H.; Fan, C.; Shi, Y.-l.; Guo, X. Walnut shell-derived hierarchical porous carbon with high performances for electrocatalytic hydrogen evolution and symmetry supercapacitors. *Int. J. Hydrogen Energy* **2020**, *45*, 443.

(16) Si, W.; Zhou, J.; Zhang, S.; Li, S.; Xing, W.; Zhuo, S. Tunable N-doped or dual N, S-doped activated hydrothermal carbons derived from human hair and glucose for supercapacitor applications. *Electrochim. Acta* **2013**, *107*, 397.

(17) Zhang, Q.; Han, K.; Li, S.; Li, M.; Li, J.; Ren, K. Synthesis of garlic skin-derived 3D hierarchical porous carbon for high-performance supercapacitors. *Nanoscale* **2018**, *10*, 2427.

(18) Jin, H.; Li, J.; Yuan, Y.; Wang, J.; Lu, J.; Wang, S. Recent progress in biomass-derived electrode materials for high volumetric performance supercapacitors. *Adv. Energy Mater.* **2018**, *8*, 1801007.

(19) Deng, Y.; Xie, Y.; Zou, K.; Ji, X. Review on recent advances in nitrogen doped carbons: preparations and applications in supercapacitors. *J. Mater. Chem. A* **2016**, *4*, 1144.

(20) Paraknowitsch, J. P.; Thomas, A. Doping carbons beyond nitrogen: an overview of advanced heteroatom doped carbons with boron, sulphur and phosphorus for energy applications. *Energy Environ. Sci.* **2013**, *6*, 2839.

(21) Liang, J.-Y.; Wang, C.-C.; Lu, S.-Y. Glucose-derived nitrogen-doped hierarchical hollow nest-like carbon nanostructures from a novel template-free method as an outstanding electrode material for supercapacitors. *J. Mater. Chem. A* **2015**, *3*, 24453.

(22) Kondrat, S.; Pérez, C. R.; Presser, V.; Gogotsi, Y.; Kornyshev, A. A. Effect of pore size and its dispersity on the energy storage in nanoporous supercapacitors. *Energy Environ. Sci.* **2012**, *5*, 6474.

(23) Kondrat, S.; Georgi, N.; Fedorov, M. V.; Kornyshev, A. A. A superionic state in nano-porous double-layer capacitors: insights from Monte Carlo simulations. *Phys. Chem. Chem. Phys.* **2011**, *13*, 11359.

(24) Liu, Q.; Duan, Y.; Zhao, Q.; Pan, F.; Zhang, B.; Zhang, J. Direct synthesis of nitrogen-doped carbon nanosheets with high surface area and excellent oxygen reduction performance. *Langmuir* **2014**, *30*, 8238.

(25) Li, Y.; Dong, J.; Zhang, J.; Zhao, X.; Yu, P.; Jin, L.; Zhang, Q. Nitrogen-Doped Carbon Membrane Derived from Polyimide as Free-Standing Electrodes for Flexible Supercapacitors. *Small* **2015**, *11*, 3476.

(26) Zhao, G.; Chen, C.; Yu, D.; Sun, L.; Yang, C.; Zhang, H.; Sun, Y.; Besenbacher, F.; Yu, M. One-step production of O-N-S co-doped three-dimensional hierarchical porous carbons for high-performance supercapacitors. *Nano Energy* **2018**, *47*, 547.

(27) Wan, L.; Wang, J.; Xie, L.; Sun, Y.; Li, K. Nitrogen-enriched hierarchically porous carbons prepared from polybenzoxazine for high-performance supercapacitors. *ACS Appl. Mater. Interfaces* **2014**, *6*, 15583.

(28) Guan, L.; Pan, L.; Peng, T.; Gao, C.; Zhao, W.; Yang, Z.; Hu, H.; Wu, M. Synthesis of biomass-derived nitrogen-doped porous carbon nanosheets for high-performance supercapacitors. *ACS Sustainable Chem. Eng.* **2019**, *7*, 8405.

(29) Xiao, K.; Ding, L. X.; Chen, H.; Wang, S.; Lu, X.; Wang, H. Nitrogen-doped porous carbon derived from residuary shaddock peel: a promising and sustainable anode for high energy density asymmetric supercapacitors. *J. Mater. Chem. A* **2015**, *4*, 372.

(30) Wang, B.; Wang, Y.; Peng, Y.; Wang, X.; Wang, N.; Wang, J.; Zhao, J. Nitrogen doped biomass-based hierarchical porous carbon with large mesoporous volume for application in energy storage. *Chem. Eng. J.* **2018**, *348*, 850−859.

(31) Zhang, W.; Wang, J.; Bao, L.; Gao, Z.; Yu, J. Nanopores created by carbon onion conductive agent providing enhanced capacitance in supercapacitors. *Diam. Relat. Mater.* **2019**, *96*, 231.

(32) Zhang, X.; Zhang, R.; Xiang, C.; Liu, Y.; Zou, Y.; Chu, H.; Qiu, S.; Xu, F.; Sun, L. Polydopamine-assisted formation of Co_3O_4-nanocube-anchored reduced graphene oxide composite for high-performance supercapacitors. *Ceram. Int.* **2019**, *45*, 13894.

(33) Zhang, J.; Chen, H.; Bai, J.; Xu, M.; Luo, C.; Yang, L.; Bai, L.; Wei, D.; Wang, W.; Yang, H. N-doped hierarchically porous carbon derived from grape marcs for high-performance supercapacitors. *J. Alloys Compd.* **2021**, *854*, 157207.

(34) Mehare, M. D.; Deshmukh, A. D.; Dhoble, S. J. Preparation of porous agrowaste-derived carbon from onion peel for supercapacitor application. *J. Mater. Sci.* **2020**, *55*, 4213−4224.

(35) Ding, C.; Liu, T.; Yan, X.; Huang, L.; Ryu, S.; Lan, J.; Yu, Y.; Zhong, W.-H.; Yang, X. An Ultra-microporous Carbon Material Boosting Integrated Capacitance for Cellulose-Based Supercapacitors. *Nano-Micro Lett.* **2020**, *12*, 63.

(36) Selvaraj, A. R.; Kim, H.-J.; Senthil, K.; Prabakar, K. Cation intercalated one-dimensional manganese hydroxide nanorods and hierarchical mesoporous activated carbon nanosheets with ultrahigh capacitance retention asymmetric supercapacitors. *Colloid Interface Sci.* **2020**, *566*, 485−494.

https://dx.doi.org/10.1021/acsomega.0c06171
ACS Omega 2021, 6, 7615−7625

(37) Chen, T.; Tang, Y.; Qiao, Y.; Liu, Z.; Guo, W.; Song, J.; Mu, S.; Yu, S.; Zhao, Y.; Gao, F. All-solid-state high performance asymmetric supercapacitors based on novel MnS nanocrystal and activated carbon materials. *Sci. Rep.* **2016**, *6*, 23289.
(38) Gandla, D.; Chen, H.; Tan, D. Q. Mesoporous structure favorable for high voltage and high energy supercapacitor based on green tea waste-derived activated carbon. *Mater. Res. Express* **2020**, *7*, 085606.
(39) Dai, P.; Zhang, S.; Liu, H.; Yan, L.; Gu, X.; Li, L.; Liu, D.; Zhao, X. Cotton fabrics-derived flexible nitrogen-dope d activate d carbon cloth for high-performance supercapacitors in organic electrolyte. *Electrochim. Acta* **2020**, *354*, 136717.
(40) Shang, T.; Xu, Y.; Li, P.; Han, J.; Wu, Z.; Tao, Y.; Yang, Q.-H. A bio-derived sheet-like porous carbon with thin-layer pore walls for ultrahigh-power supercapacitors. *Nano Energy* **2020**, *70*, 104531.
(41) Thangavel, R.; Kannan, A. G.; Ponraj, R.; Thangavel, V.; Kim, D.-W.; Lee, Y.-S. High-energy green supercapacitor driven by ionic liquid electrolytes as an ultra-high stable next-generation energy storage device. *J. Power Sources* **2018**, *383*, 102−109.
(42) Rani, M. U.; Nanaji, K.; Rao, T. N.; Deshpande, A. S. Corn husk derived activated carbon with enhanced electrochemical performance for high-voltage supercapacitors. *J. Power Sources* **2020**, *471*, 228387.
(43) Yu, F.; Ye, Z.; Chen, W.; Wang, Q.; Wang, H.; Zhang, H.; Peng, C. Plane tree bark-derived mesopore-dominant hierarchical carbon for high voltage supercapacitors. *Appl. Surf. Sci.* **2020**, *507*, 145190.
(44) Nomura, K.; Nishihara, H.; Kobayashi, N.; Asada, T.; Kyotani, T. 4.4 V Supercapacitors Based on Super-stable Mesoporous Carbon Sheet Made of Edge-free Graphene Walls. *Energy Environ. Sci.* **2019**, *12*, 1542−1549.
(45) Lyklema, J. *Fundamentals of Interface and Colloid Science 2*; Academic Press: New York, 1995.
(46) Ren, G.; Li, Y.; Chen, Q.; Qian, Y.; Zheng, J.; Zhu, Y.; Teng, C. Sepia-derived, P Co-doped porous carbon spheres as oxygen reduction reaction electrocatalyst and supercapacitor. *ACS Sustainable Chem. Eng.* **2018**, *6*, 16032.
(47) Liu, B.; Liu, Y.; Chen, H.; Yang, M.; Li, H. Oxygen and nitrogen co-doped porous carbon nanosheets derived from perilla frutescens for high volumetric performance supercapacitors. *J. Power Sources* **2017**, *341*, 309.
(48) Han, X.; Jiang, H.; Zhou, Y.; Hong, W.; Zhou, Y.; Gao, P.; Ding, R.; Liu, E. High performance nitrogen-doped porous activated carbon for supercapacitor derived from pueraria. *J. Alloys Compd.* **2018**, *744*, 544.
(49) Ji, L.; Wang, B.; Yu, Y.; Wang, N.; Zhao, J. S co-doped biomass derived carbon with sheet-like microstructures for supercapacitors. *Electrochim. Acta* **2020**, *331*, 135348.
(50) Yan, J.; Fang, Y.-Y.; Wang, S.-W.; Wu, S.-W.; Wang, L. −X.; Zhang, Y.; Luo, H.-W.; Cao, Y.; Gao, H.-L.; Wang, L.-Z.; Liu, F.-J. Nitrogen-doped oxygen-rich activated carbon derived from Longan shell for supercapacitors. *Int. J. Electrochem. Sci.* **2020**, *15*, 1982.

https://dx.doi.org/10.1021/acsomega.0c06171
ACS Omega 2021, 6, 7615−7625